



Genesis of the Hermyingyi W–Sn deposit, Southern Myanmar, SE Asia: Constraints from fluid inclusion and multiple isotope (C, H, O, S, and Pb) studies

Hai Jiang¹ · Shao-Yong Jiang¹ · Wen-Qian Li² · Kui-Dong Zhao¹ · Wei Zhang¹ · Qiang Zhang¹

Received: 19 September 2021 / Accepted: 14 February 2022 / Published online: 22 February 2022
© The Author(s), under exclusive licence to Springer-Verlag GmbH Germany, part of Springer Nature 2022

Abstract

The Hermyingyi quartz vein–type W–Sn deposit is one of the major tungsten and tin producers in Myanmar. It comprises a series of north-trending wolframite–cassiterite-bearing quartz veins mainly hosted in the Late Cretaceous monzogranite which intruded into Paleozoic metasedimentary rocks. Conventional fluid inclusion and infrared microthermometric results reveal that homogenization temperatures decrease from the wolframite–cassiterite stage (stage I, 239–348 °C) through the sulfide stage (stage II, 222–248 °C) to the barren quartz vein stage (stage III, 174–218 °C), whereas salinities vary in a similar range for stage I (1.4–11.7 wt% NaCl equiv.) and II (1.7–11.3 wt% NaCl equiv.) and are slightly lower in stage III (0.7–5.9 wt% NaCl equiv.). Fluid inclusions in wolframite and cassiterite from stage I have similar salinities but distinctly higher (~60 °C) temperatures compared to those in coexisting quartz. The $\delta^{18}\text{O}_{\text{fluid}}$ (3.3 to 7.0‰) and δD (–76 to –61‰) values of quartz, wolframite, and cassiterite indicate a dominantly magmatic fluid in stage I, while decreasing values of quartz in stage II ($\delta^{18}\text{O}_{\text{fluid}} = 1.3$ to 1.8‰, $\delta\text{D} = -81$ to -71 ‰) and III ($\delta^{18}\text{O}_{\text{fluid}} = -3.1$ to -1.6 ‰, $\delta\text{D} = -89$ to -73 ‰) show a trend of cooling and dilution by meteoric water. The negative and increasing $\delta^{13}\text{C}_{\text{CO}_2}$ values (from -20.5 to -4.9 ‰) of quartz fluid inclusions from early to late stages imply that organic carbon was added to the magmatic fluid through fluid–rock interaction in stage I, consumed with time and almost exhausted in stage III. The $\delta^{34}\text{S}$ values (1.6 to 7.9‰) of sulfides coupled with the comparable Pb isotope data of the monzogranite ($^{206}\text{Pb}/^{204}\text{Pb} = 18.572 - 18.784$, $^{207}\text{Pb}/^{204}\text{Pb} = 15.749 - 15.760$, $^{208}\text{Pb}/^{204}\text{Pb} = 39.265 - 39.333$) and sulfides ($^{206}\text{Pb}/^{204}\text{Pb} = 18.655 - 18.749$, $^{207}\text{Pb}/^{204}\text{Pb} = 15.737 - 15.768$, $^{208}\text{Pb}/^{204}\text{Pb} = 39.258 - 39.368$) suggest igneous sources of sulfur and lead. By combining these results, we propose that fluid–rock interaction and fluid cooling have been responsible for the deposition of wolframite and cassiterite in the Hermyingyi deposit.

Keywords Fluid inclusion, Infrared microthermometry · H–O–C–S–Pb isotopes · the Hermyingyi W–Sn deposit · Southern Myanmar · Southeast Asia

Introduction

Tungsten (W) and tin (Sn) are two critical metals that have emerged as an indispensable part of various industrial applications, particularly the high-tech industry (Jiang et al. 2020). Globally, Phanerozoic W–Sn mineralization occurs mainly along the margins of Gondwana-derived blocks (Romer and Kroner 2016) and shows a close spatial association with highly evolved peraluminous granites, which are generally considered the prime source of metals and mineralizing fluids (Heinrich 1990; Hulsbosch et al. 2016; Jiang et al. 2017, 2018, 2019a, 2019b, 2020; Lehmann 2021; Ni et al. 2020). These granite-related W–Sn deposits display a diversity of mineralization styles, e.g., vein, greisen, breccia, pegmatite, and skarn types, which may be correlated

Editorial handling: D. Zhai

✉ Shao-Yong Jiang
shyjiang@cug.edu.cn

¹ State Key Laboratory of Geological Processes and Mineral Resources, School of Earth Resources, Collaborative Innovation Center for Exploration of Strategic Mineral Resources, China University of Geosciences, Wuhan 430074, China

² Key Laboratory of Mineralogy and Metallogeny, Guangzhou Institute of Geochemistry, Chinese Academy of Sciences, Guangzhou 510640, China

with the depth of granite emplacement (Linnen 1998). Despite a general consensus that the progressive evolution from magmatic through magmatic-hydrothermal transitional to hydrothermal conditions has been responsible for the concentration, transport, and deposition of W and Sn, the mechanism(s) effectively leading to ore deposition remain(s) an open issue. Fluid mixing, cooling, boiling, and fluid-rock interaction have been proposed as major processes for W–Sn ore formation (Heinrich 1990; Ni et al. 2015, 2020; Lecumberri-Sanchez et al. 2017; Korges et al. 2018; Jiang et al. 2019b, 2020; Wang et al. 2019).

Southeast Asia is well known for its tin(-tungsten) endowment. The Sn(-W) deposits and occurrences, intimately associated with Early Permian to Eocene granitic magmatism widespread in the Indochina-East Malay and Sibumasu blocks (Cobbing et al. 1986; Mitchell et al. 2012; Ng et al. 2015; Gardiner et al. 2017; Jiang et al. 2017, 2021; Li et al. 2018, 2019; Myint et al. 2018; Mao et al. 2020; Yang et al. 2020), define the famous Southeast Asian Tin Belt (SATB), a belt 2800 km long and 400 km wide that extends from Indonesia in the south through Malaysia and Thailand to Myanmar in the north (Electronic Supplementary Material: ESM Fig. 1; Schwartz et al. 1995). Primary Sn deposits are mainly distributed in the western SATB, particularly in central and southern Myanmar, where some Sn deposits exhibit equally or more important than W mineralization (Fig. 1). The Hermyingyi W–Sn deposit, representative of quartz vein-type mineralization, has more than 100 years of mining history and is one of the major tungsten and tin producers in Myanmar. So far, only a few studies have been dedicated to the ore genesis of this historic deposit. Our geochronological data yielded a molybdenite Re–Os isochron age of 68.4 ± 2.5 Ma (Jiang et al. 2019a), coincident with the emplacement age of the Hermyingyi monzogranite (70.0 ± 0.4 Ma; Jiang et al. 2017). These overlapping ages confirm a close relationship between W–Sn mineralization and granitic magmatism in the Hermyingyi deposit. A preliminary sulfur isotope study ($\delta^{34}\text{S} = +1.9$ to $+5.6\%$) suggested a magmatic origin for sulfur (Jiang et al. 2019a). However, some basic issues concerning the fluid and metal source, the evolution of the mineralizing fluid, and the mineralization process of the Hermyingyi deposit remain poorly understood. Unraveling these issues may have a broader implication for understanding and exploring W–Sn deposits in Myanmar and beyond.

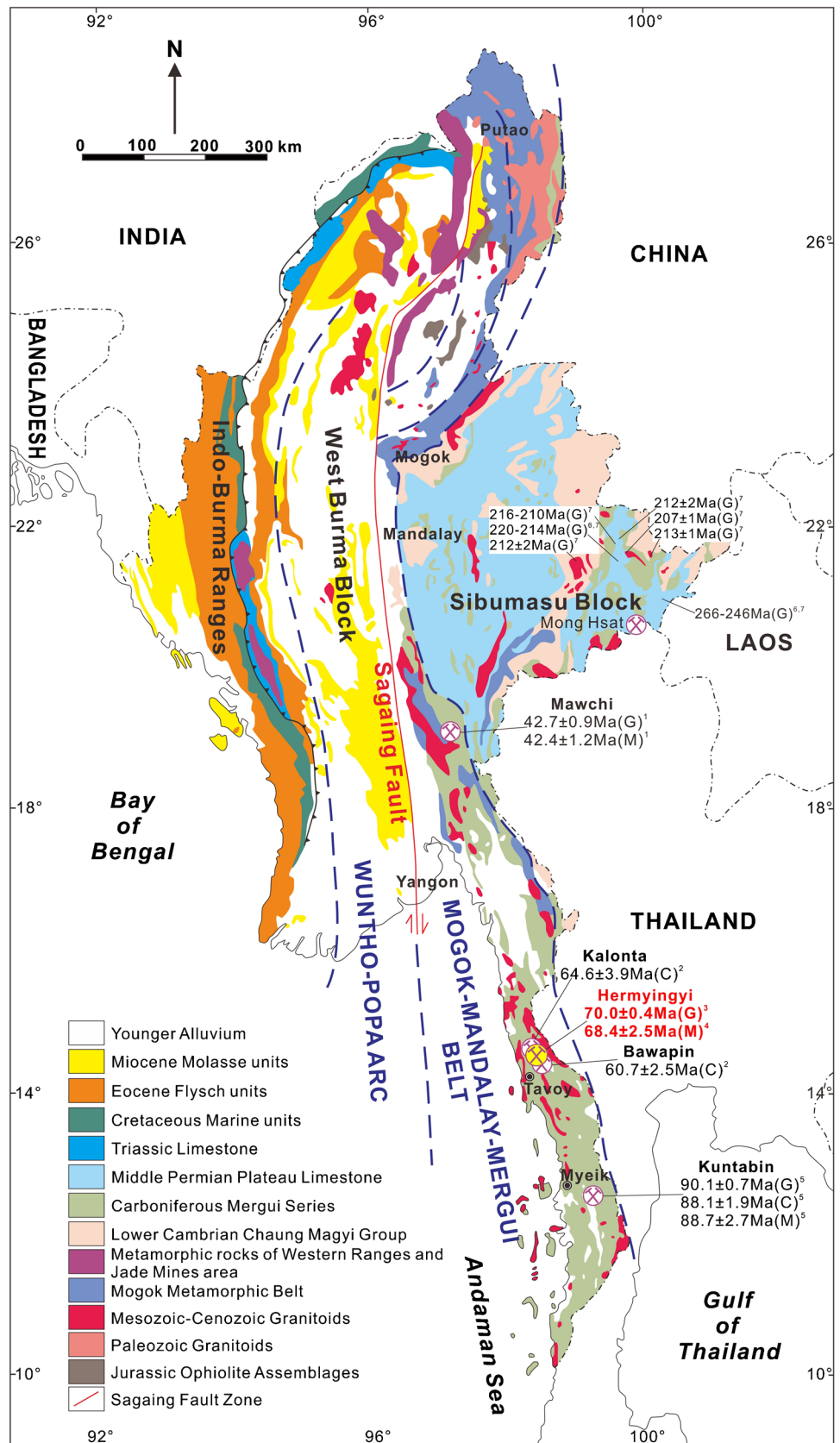
In this paper, we conduct a comprehensive study of the Hermyingyi W–Sn deposit in terms of fluid inclusions in coexisting quartz, wolframite, and cassiterite, and in situ sulfur isotope analysis as well as other isotope analyses (C, H, O, and Pb). Combining these new data with the previously published data and regional geologic constraints, we aim to trace the source of metals and mineralizing fluids and decipher the mechanism triggering ore deposition.

Geological setting

Myanmar lies primarily on two Gondwana-derived continental blocks: the Sibumasu Block in the east and the West Burma Block in the west, which are bounded by the N–S trending Sagaing Fault (Fig. 1; Barber and Crow 2009; Mitchell et al. 2012). The Mesozoic–Cenozoic geology of the West Burma Block is characterized by the development of the Wuntho–Popa Arc on the pre-Mesozoic basement, which underwent two periods of magmatic flare-ups at ca. 110–80 and 70–40 Ma (Mitchell et al. 2012; Wang et al. 2014; Gardiner et al. 2017; Lin et al. 2019). To the west of the West Burma Block lies the Indo-Burma Ranges, consisting mainly of Upper Triassic turbidites, Lower Eocene flysch deposits (Mitchell et al. 2012), and discontinuous ophiolite occurrences (e.g., Kalaymyo, Chin Hill and Naga Hill ophiolites), which are dated at ca. 127 Ma and suggested as representing the Neo-Tethyan suture zone in Myanmar that could be correlated with the Yarlung–Tsangpo suture zone in Tibet, China (Liu et al. 2016). It has been suggested that the Sibumasu Block was detached from Gondwana in the late Early Permian (Metcalf 2013), covering northeastern Sumatra, western Peninsular Malaysia, western Thailand, and eastern Myanmar (ESM Fig. 1). In Myanmar, the Sibumasu Block is represented mainly by Upper Carboniferous–Lower Permian metasedimentary rocks (the Mergui Series) in its southern part, Middle Permian Plateau limestones in its central and eastern parts, and the Mogok metamorphic belt along its western margin which has been interpreted as a response to a regional Eocene–Oligocene (ca. 47–29 Ma) metamorphic event (Searle et al. 2007). The granites, mainly emplaced between 128 and 17 Ma (Mitchell et al. 2012; Gardiner et al. 2017; Jiang et al. 2017; Li et al. 2018, 2019; Myint et al. 2018; Mao et al. 2020), occur throughout the Sibumasu Block within Myanmar, defining a N–S trending belt stretching at least from Mogok in the north through Tavoy to Myeik in the south (Fig. 1). These Cretaceous–Neogene granites constitute the main part of the Western Province of Cobbing et al. (1986). In addition, the granites of the Eastern Province and the Main Range Province were recently reported in eastern Myanmar, adjacent to the Thai–Myanmar border (Fig. 1), with zircon U–Pb ages of 266–246 and 220–207 Ma, respectively (Gardiner et al. 2016; Cong et al. 2021).

The W–Sn deposits and occurrences are not uniformly distributed in Myanmar. The Mawchi W–Sn deposit, the largest primary W–Sn deposit in Myanmar, is located in the Kayah State, central Myanmar (Fig. 1). A recent geochronological study suggested that W–Sn mineralization and related granitic magmatism in the Mawchi deposit occurred synchronously at ca. 42 Ma (Myint et al. 2018).

Fig. 1 Simplified geological map showing major blocks and the granite belts of Myanmar (modified after Gardiner et al. 2014). Typical W–Sn deposits are also shown. Abbreviations: G, granite; M, molybdenite; C, cassiterite. Ages of W–Sn mineralization and related granitic magmatism are from 1, Myint et al. (2018); 2, Li et al. (2018); 3, Jiang et al. (2017); 4, Jiang et al. (2019a); 5, Mao et al. (2020). Ages of Permo-Triassic granites are from 6, Gardiner et al. (2016); 7, Cong et al. (2021)



According to Than Htun et al. (2017), the eastern Shan State (eastern Myanmar) is a promising area that deserves further detailed exploration, where the Mong Hsat primary Sn deposit hosted by Late Triassic (ca. 214 Ma) biotite granite was discovered in 2011 (Fig. 1). Apart from these, more than 50 primary Sn–W deposits, including the largest tin placer deposit in Myanmar (the Heinda deposit), cluster in the Tavoy district, southern Myanmar, making it the most important tin-tungsten-producing area in Myanmar (Than Htun et al. 2017). The strata exposed in southern Myanmar are dominated by the Mergui Series (Mitchell et al. 2012), which is equivalent to the Upper Carboniferous–Lower Permian Phuket Group in Peninsular Thailand, a thick sequence of rift-infill sediments containing a high proportion of glacially derived diamictites (Ridd 2009). Quartz vein-type W–Sn mineralization is prevailing in the Tavoy district, spatially associated with the granites, e.g., the Hermyingyi, Bawapin, and Kalonta W–Sn deposits. Limited numbers of radiometric dating of ore minerals including U/Pb on cassiterite and Re/Os on molybdenite revealed a Late Cretaceous–Paleocene (ca. 68–61 Ma) W–Sn mineralization event (Li et al. 2018; Jiang et al. 2019a), temporally coincident with ca. 70–52-Ma granitic magmatism in the Tavoy district and nearby (Gardiner et al. 2017; Jiang et al. 2017; Li et al. 2019). Further south is the Myeik district, where several alluvial and primary Sn–W deposits are distributed, e.g., the Thabawleik alluvial deposit, and the Kuntabin and Laytha Taung primary deposits (Than Htun et al. 2017; Mao et al. 2020). Based on the results of cassiterite U–Pb and molybdenite Re–Os dating, Mao et al. (2020) recently

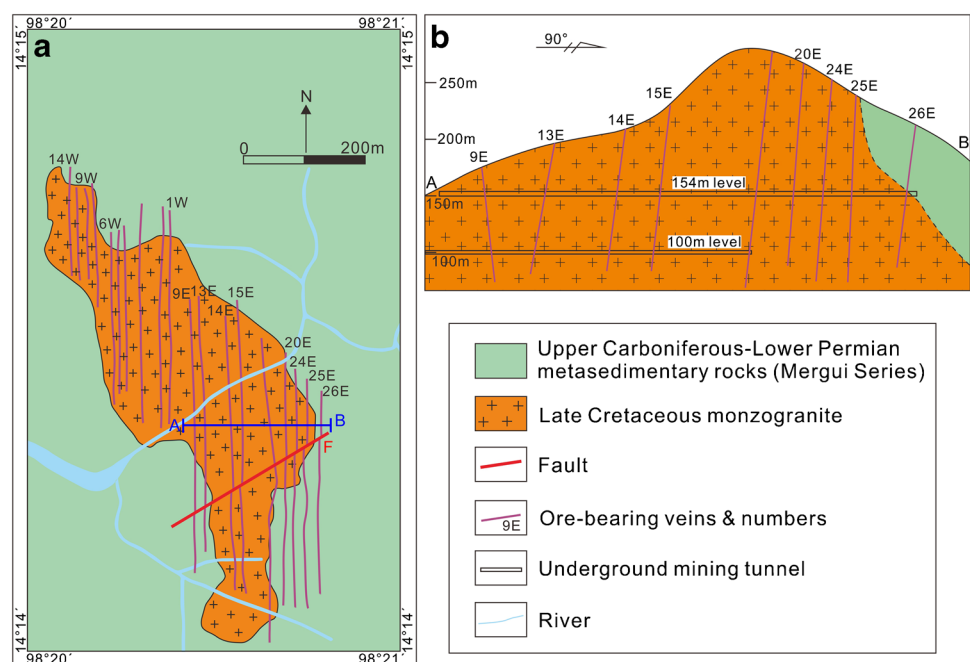
suggested that the Kuntabin Sn–W deposit formed at ca. 88 Ma, genetically associated with the coeval (ca. 90 Ma) two-mica granite exposed in the mine.

Deposit geology

The Hermyingyi W–Sn deposit is located ~40 km northeast of Tavoy Township (Fig. 1). Based on Jiang et al. (2019a), we herein briefly summarize the geology of the Hermyingyi W–Sn deposit. The sedimentary country rocks consist of the Mergui Series, a thick sequence of Upper Carboniferous to Lower Permian metasediments locally intercalated with volcanic tuffs and agglomerates. The Hermyingyi granite occurs as a stock at least 1.4 km in length and up to 0.5 km in width (Fig. 2(a)) and intrudes the metasedimentary rocks with sharp contacts (Fig. 4a). Recent zircon U–Pb dating indicated that the granite was emplaced at ca. 70 Ma (Jiang et al. 2017). The Hermyingyi granite is a medium- to fine-grained monzogranite consisting mainly of plagioclase (~35 vol%), K-feldspar (~30 vol%), quartz (~25 vol%), muscovite (~5 vol%), and biotite (~5 vol%), and was interpreted as A-type granite generated in a back-arc extensional setting triggered by rollback of the Neo-Tethyan slab (Jiang et al. 2017).

W–Sn mineralization at Hermyingyi comprises a series of subparallel quartz-wolframite-cassiterite veins, which strike nearly north–south and dip steeply to the east or the west and are hosted in the Hermyingyi granite and the surrounding metasediments (Fig. 2). More than 300 quartz veins with variable thickness from several mm to 2 m are documented in the Hermyingyi deposit, but only 15 of them are in

Fig. 2 (a) Geological map of the Hermyingyi W–Sn deposit (modified after Jiang et al. 2019a). (b) Cross section of the Hermyingyi deposit



production (Than Htun et al. 2017; Jiang et al. 2019a). The ore minerals consist mainly of wolframite and cassiterite, and some sulfide minerals such as molybdenite, pyrite, chalcopyrite, galena, sphalerite, and bismuthinite. The gangue minerals are mainly quartz, muscovite, and fluorite. Jiang et al. (2019a) recently reported a Re–Os isochron age of 68.4 ± 2.5 Ma for molybdenite associated with W–Sn mineralization at Hermyingyi. The Hermyingyi W–Sn deposit in Myanmar shows two main differences with respect to the W–Sn deposits in South China (e.g., Jiang et al. 2019b): (1) unlike the W–Sn deposits in South China which are mainly hosted in the surrounding metasedimentary rocks, the ore veins at Hermyingyi are mainly hosted within the granite body; and (2) arsenopyrite appears to be absent in the Hermyingyi W–Sn deposit, contrary to what is commonly found in the W–Sn deposits in South China.

Jiang et al. (2019a) recognized three main mineralization stages at Hermyingyi: the wolframite-cassiterite stage (stage I), followed by the sulfide stage (stage II) and the barren quartz vein stage (stage III) (Fig. 3). Stage I is dominated by massive quartz, wolframite, and cassiterite with trace amounts of sulfides (Fig. 4c–e). Wolframite commonly occurs as the tabular or needle crystal (Fig. 4b–c) and is locally found as nodules. In some cases, chalcopyrite is enclosed in wolframite (Fig. 5a). Cassiterite occurs as well-zoned crystals (Fig. 5b) commonly intergrown with or

slightly earlier than wolframite (Fig. 5c, d, g). Molybdenite appears to be the earliest formed sulfide that is present as lamellar or tabular crystals (Fig. 4d–e) with kink-like structure (Fig. 5e). Despite the occasional occurrence in the center of the quartz veins, both wolframite and cassiterite occur mainly along the vein walls (Fig. 4b, c), possibly indicating that they were deposited slightly earlier than the coexisting quartz. Stage II crosscuts stage I and is characterized by deposition of abundant sulfides with minor wolframite and cassiterite (Figs. 4f, g, 5c, f–i). Euhedral or subhedral pyrite grains are commonly intergrown with sphalerite and chalcopyrite (chalcopyrite disease) (Fig. 5h, i). Sphalerite generally occurs as fine-grained aggregates closely associated with chalcopyrite or galena (Fig. 4g). Some sphalerite grains are dispersed as droplets in chalcopyrite (Fig. 5i). Stage III is characterized by the occurrence of barren quartz and fluorite (Fig. 4h, i). The dominant hydrothermal alteration is greisenization, which is intense and pervasive at Hermyingyi and developed mainly on both sides of the ore-bearing veins (Fig. 4b–d). The greisen consists mainly of quartz and muscovite. Interestingly, the thickness of the greisen zones varies significantly and is proportional to the vein width to only a limited extent.

Sampling and analytical methods

More than 60 samples were collected from the 190-, 154-, and 100-m mine levels of the Hermyingyi deposit. Quartz samples from stages I, II, and III were used for fluid inclusion study and C–H–O isotope analyses. Samples of wolframite and cassiterite from stage I were used for fluid inclusion study and O isotope analysis. Thin sections of sulfides were used for in situ sulfur isotope analysis. Sulfide mineral separates and the granite samples which were previously studied by Jiang et al. (2017) were used for Pb isotope analysis.

A laser Raman spectroscopic study on individual inclusions of quartz from stages I, II, and III was conducted at the State Key Laboratory of Geological Processes and Mineral Resources, China University of Geosciences (GPMR-CUG), using a Renishaw RM-1000 Raman microprobe. An argon (532.5 nm) laser with a surface power of 2 mW was employed as the laser source. The microthermometric measurement of quartz was conducted using a Linkam THMSG600 heating/freezing stage coupled to a Leica DM 2500p microscope at Collaborative Innovation Center for Exploration of Strategic Mineral Resources, China University of Geosciences. The microthermometric data of wolframite and cassiterite were obtained via a Linkam THMSG600 heating/freezing stage coupled to an Olympus BX51 infrared microscope. The range of temperature measurement of the stage is from -196 to 600 °C. During the analytical procedure, the freezing or heating rate was set at

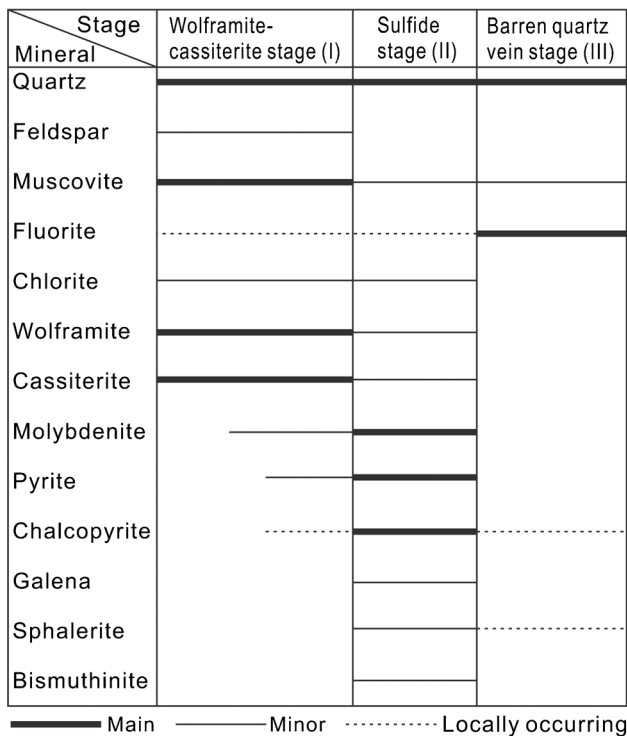


Fig. 3 Paragenesis of mineral assemblages showing the sequence of mineralization in the Hermyingyi W–Sn deposit (after Jiang et al. 2019a)

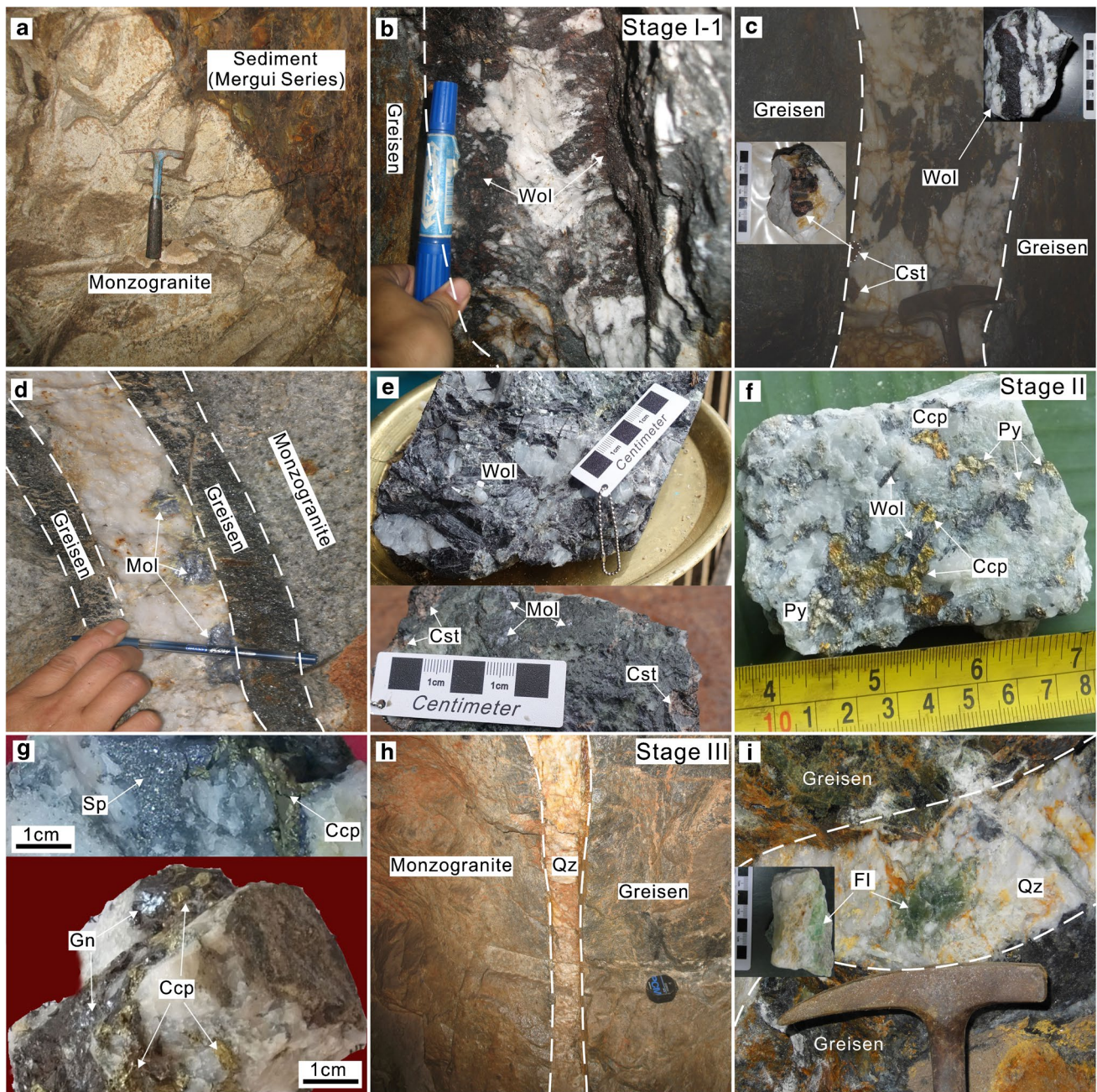


Fig. 4 **a** Granite intruding the metasedimentary rocks with sharp contacts. **b** Euhedral wolframite attached to the vein walls, with central infill of massive quartz. **c** Wolframite-cassiterite quartz vein. **d**, **e** Ore minerals of the wolframite-cassiterite stage. **f** Wolframite-bearing

quartz vein crosscut by chalcopyrite-pyrite vein. **g** Ore minerals of the sulfide stage. **h**, **i** Late-stage quartz-fluorite vein. *Ccp* chalcopyrite, *Cst* cassiterite, *Fl* fluorite, *Gn* galena, *Mol* molybdenite, *Py* pyrite, *Qz* quartz, *Sp* sphalerite, *Wol* wolframite

20 °C/min and gradually reduced to 0.1–0.5 °C/min when approaching the phase transition point.

Carbon, hydrogen, and oxygen isotope analyses were carried out at the Stable Isotope Laboratory, Institute of Mineral Resources, Chinese Academy of Geological Sciences in Beijing, using a MAT-251 mass spectrometer for C isotope analysis and a MAT-253 mass spectrometer for H–O isotope analysis. The H and C isotope values were determined

by measuring the water and CO₂ hosted by fluid inclusions of quartz, respectively. The O isotope values were obtained through direct measurement of quartz, wolframite, and cassiterite. The stable isotope analyses followed the procedures described in Zhang et al. (2013), Peng et al. (2018), and Jiang et al. (2019b). The hydrogen and oxygen isotope values were reported as per mil relative to the V-SMOW standard with the error of $\pm 2.0\%$ for δD and $\pm 0.2\%$ for $\delta^{18}O$,

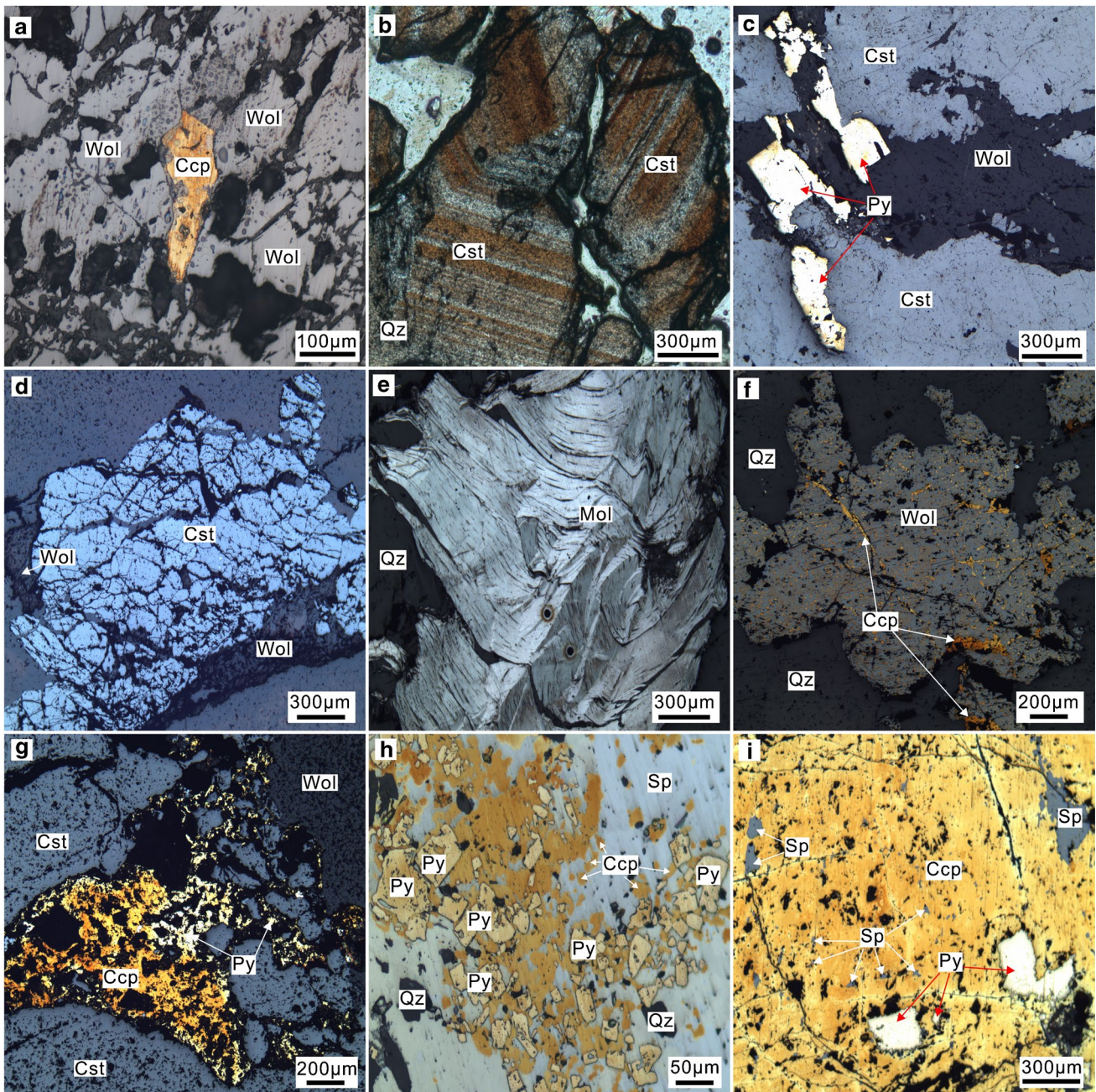


Fig. 5 Photomicrographs of ore minerals. **a** Chalcopyrite enclosed in wolframite. **b** Well-zoned cassiterite. **c** Wolframite-cassiterite quartz vein crosscut by pyrite vein. **d** Cassiterite crosscut by wolframite. **e** Molybdenite showing kink-like structure. **f** Wolframite-bearing quartz

vein crosscut by sulfide vein. **g** Wolframite-cassiterite quartz vein crosscut by sulfide vein. **h, i** Sphalerite coexisting with pyrite and chalcopyrite. *Ccp* chalcopyrite, *Cst* cassiterite, *Mol* molybdenite, *Py* pyrite, *Qz* quartz, *Sp* sphalerite, *Wol* wolframite

and the carbon isotope values were reported with respect to the V-PDB standard with the error of $\pm 0.1\text{‰}$ for $\delta^{13}\text{C}$.

In our previous study, sulfide grains were selected from unprocessed crushed samples by hand-picking, and their sulfur isotope compositions were measured through the conventional method (Jiang et al. 2019a). Herein, we obtained in situ sulfur isotope data of sulfides from different stages using a Nu Plasma II MC-ICP-MS coupled with

a Resonetics-S155 excimer ArF laser ablation system at GPMR-CUG. In order to collect the data, the spot analyses were made using a 33- μm laser beam at pulse duration of 40 s and a frequency of 10 Hz. The procedure of in situ LA-MC-ICP-MS sulfur isotope analysis has been reported in Peng et al. (2018). A sphalerite standard NBS-123 ($\delta^{34}\text{S} = +17.1\text{‰}$) and an in-house pyrite standard WS-1 ($\delta^{34}\text{S} = +1.0\text{‰}$) were used as reference material. The sulfur

isotope values were reported relative to the V-CDT standard with the error of $\pm 0.1\%$.

The lead isotope compositions of 22 sulfide and 5 granite samples were determined via a Neptune Plus MC-ICP-MS, at the State Key Laboratory for Mineral Deposits Research of Nanjing University. The analytical procedure is similar to that described by Peng et al. (2018). The Pb reference standard NBS-981 was used for the correction of reported data, with measured $^{206}\text{Pb}/^{204}\text{Pb}$, $^{207}\text{Pb}/^{204}\text{Pb}$, and $^{208}\text{Pb}/^{204}\text{Pb}$ ratios of 16.941, 15.495, and 36.706, respectively.

Results

Fluid inclusions

Petrography and microthermometry of fluid inclusions

Based on optical and infrared observations, two types of fluid inclusions (FIs) were identified in quartz and wolframite (ESM Fig. 2a–f): (1) liquid-rich two-phase FIs (L-type) and (2) vapor-rich two-phase FIs (V-type). L-type FIs are dominant in quartz and wolframite and occupy $> 95\%$ of the total inclusion numbers, while V-type FIs are subordinate and contribute to $\sim 5\%$ of the total inclusion numbers. FIs in cassiterite are dominated by L-type FIs, which contain $< 50\%$ vapor bubbles (ESM Fig. 2g–i). In this study, the microthermometric measurements were carried out either on the isolated inclusions thought to be primary (Roedder 1984) or on a cluster of FIs with similar heating-freezing behavior which together represent fluid inclusion assemblages (FIA) (Goldstein and Reynolds 1994). Almost all the analyzed FIs are ellipsoid, negative crystal, or elongated in shape and 6 to 20 μm in size (ESM Fig. 2). The microthermometric results are presented in ESM Table 1.

Wolframite-cassiterite stage (stage I) L-type and V-type FIs in wolframite of stage I homogenized to liquid, with T_h of 296–348 $^\circ\text{C}$ and salinities of 2.7–10.6 wt% NaCl equiv. for L-type FIs and T_h of 302–342 $^\circ\text{C}$ and salinities of 5.3–11.7 wt% NaCl equiv. for V-type FIs (Fig. 6(a, b)). Only L-type FIs were recognized in cassiterite, which have similar T_h (296–346 $^\circ\text{C}$) and a smaller range of salinities (2.6–8.0 wt% NaCl equiv.) compared to FIs in wolframite (Fig. 6(a, b)). In comparison, FIs in quartz have distinctly lower T_h but comparable salinities. Both L-type and V-type FIs in quartz homogenized to liquid. L-type FIs have homogenization temperatures (T_h) of 239–276 $^\circ\text{C}$ and ice-melting temperatures ($T_{m,ice}$) of -6.5 to -0.8 $^\circ\text{C}$, corresponding to salinities of 1.4–9.9 wt% NaCl equiv., while V-type FIs yield T_h of 248–263 $^\circ\text{C}$ and salinities of 5.0–8.3 wt% NaCl equiv. (ESM Table 1; Fig. 6(c, d)).

Sulfide stage (stage II) Quartz of stage II contains L-type and V-type FIs, which homogenized to liquid. L-type FIs have T_h of 222–248 $^\circ\text{C}$ and salinities of 1.7–11.3 wt% NaCl equiv., while V-type FIs have T_h of 231–236 $^\circ\text{C}$ and salinities of 3.7–6.2 wt% NaCl equiv. (Fig. 6(e, f)). Overall, FIs in quartz of stage II have lower T_h but similar salinities when compared to those in stage I quartz.

Barren quartz vein stage (stage III) Only L-type FIs were found in quartz of stage III, which homogenized to liquid. Their T_h and salinities range from 174 to 218 $^\circ\text{C}$ and 0.7 to 5.9 wt% NaCl equiv., respectively (Fig. 6(g, h)), distinctly lower than those of FIs in quartz of stage I and II and in wolframite and cassiterite of stage I (ESM Table 1).

Laser Raman spectroscopy

Raman spectra for the vapor phase reveal that FIs in quartz of stage I contain only CH_4 (Fig. 7a) and FIs in quartz of stage II contain both CH_4 and CO_2 (Fig. 7b, c); only CO_2 was detected from FIs in quartz of stage III (Fig. 7d). Interestingly, despite the presence of CO_2 in the vapor phases, no CO_2 -bearing FIs were observed petrographically.

Hydrogen, oxygen, and carbon isotopes

In stage I, the measured δD and $\delta^{18}\text{O}$ values of quartz range from -76 to -61% and from 12.0 to 13.9 $\%$, respectively; the calculated $\delta^{18}\text{O}_{\text{fluid}}$ values of quartz range from 3.3 to 5.2 $\%$ (ESM Table 2; Fig. 8(a)). Wolframite and cassiterite in this stage have calculated $\delta^{18}\text{O}_{\text{fluid}}$ values of 4.6–5.5 $\%$ and 6.0–7.0 $\%$, respectively (ESM Table 2; Fig. 8(b)). In stage II, the measured δD and $\delta^{18}\text{O}$ values of quartz range from -81 to -71% and from 11.1 to 11.6 $\%$, respectively; the calculated $\delta^{18}\text{O}_{\text{fluid}}$ values of quartz range from 1.3 to 1.8 $\%$ (ESM Table 2; Fig. 8(a)). In stage III, the measured δD and $\delta^{18}\text{O}$ values of quartz range from -89 to -73% and from 9.3 to 10.8 $\%$, respectively; the calculated $\delta^{18}\text{O}_{\text{fluid}}$ values of quartz range from -3.1 to -1.6% (ESM Table 2; Fig. 8(a)).

CO_2 extracted from FIs of quartz have $\delta^{13}\text{C}_{\text{CO}_2}$ values of -20.5 to -12.1% (stage I), -16.5 to -15.4% (stage II), and -10.2 to -4.9% (stage III) (ESM Table 2; Fig. 9).

Sulfur and lead isotopes

Sulfides from stage I have $\delta^{34}\text{S}$ values ranging from 3.2 to 7.9 $\%$, including values of molybdenite (3.2–4.3 $\%$; $n=7$, average = 3.6 $\%$), chalcopyrite (6.2–7.9 $\%$; $n=6$, average = 7.1 $\%$), and pyrite (5.7–7.7 $\%$; $n=5$, average = 6.6 $\%$) (ESM Table 3; Fig. 10). Sulfides from stage II have slightly lower $\delta^{34}\text{S}$ values ranging from 1.6 to 4.5 $\%$, which were obtained from molybdenite (1.6–2.3 $\%$; $n=4$,

Fig. 6 Histograms of homogenization temperatures and salinities of fluid inclusions and salinities of fluid inclusions from different mineralization stages in the Hermyingyi W–Sn deposit

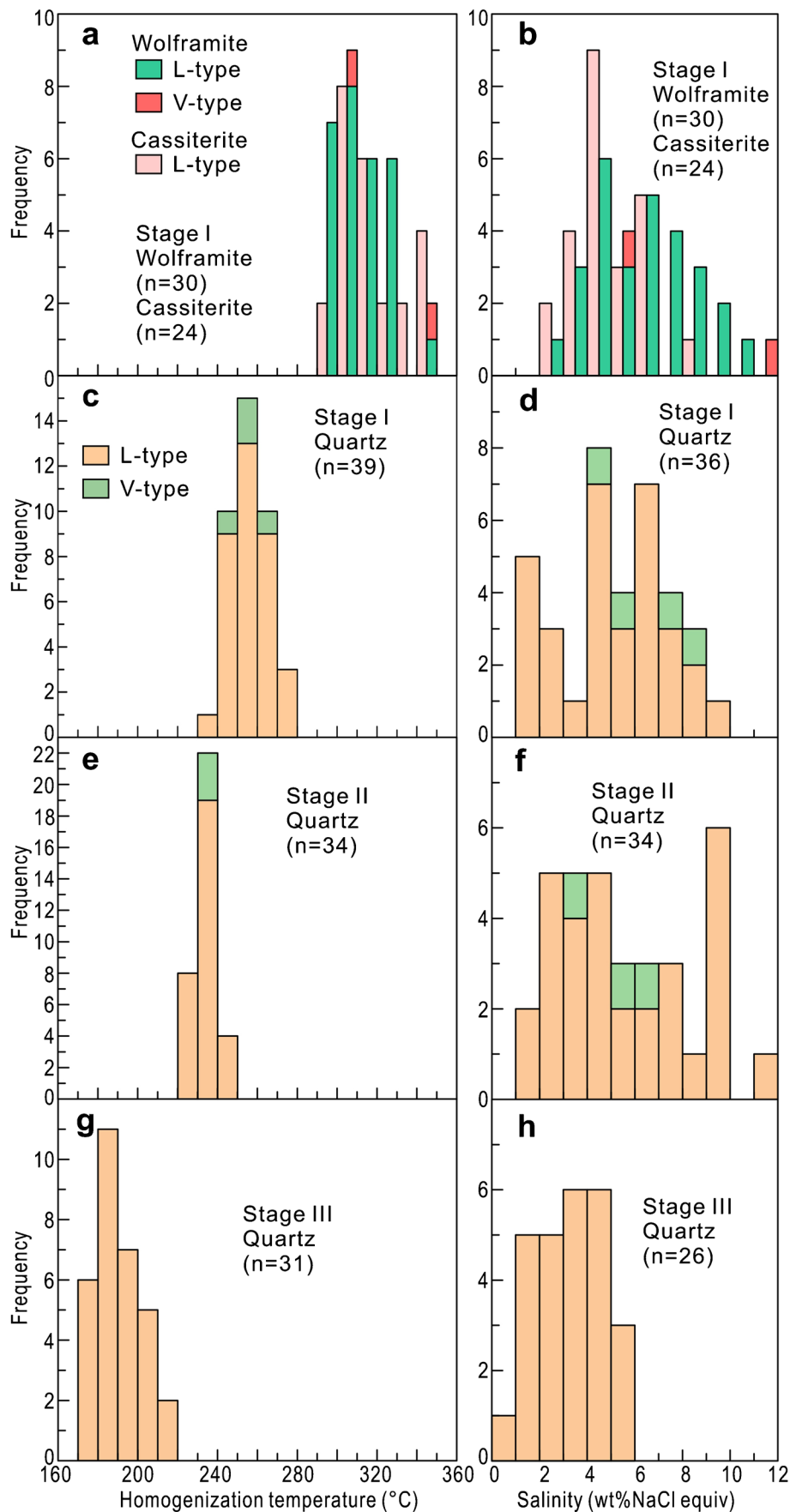


Fig. 7 Representative Laser Raman analysis of fluid inclusions in quartz of different mineralization stages from the Hermyingyi W–Sn deposit. **a** L-type fluid inclusion in stage I quartz. **b, c** L-type fluid inclusions in stage II quartz. **d** L-type fluid inclusion in stage III quartz

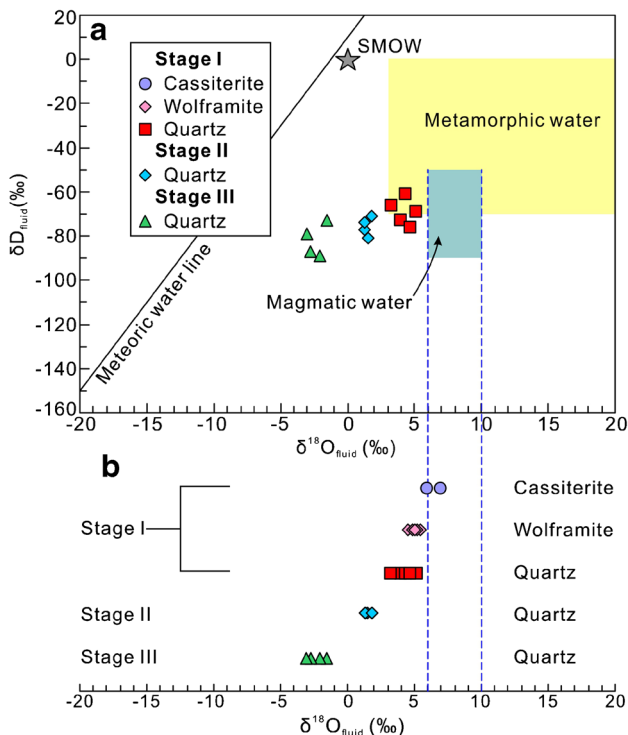
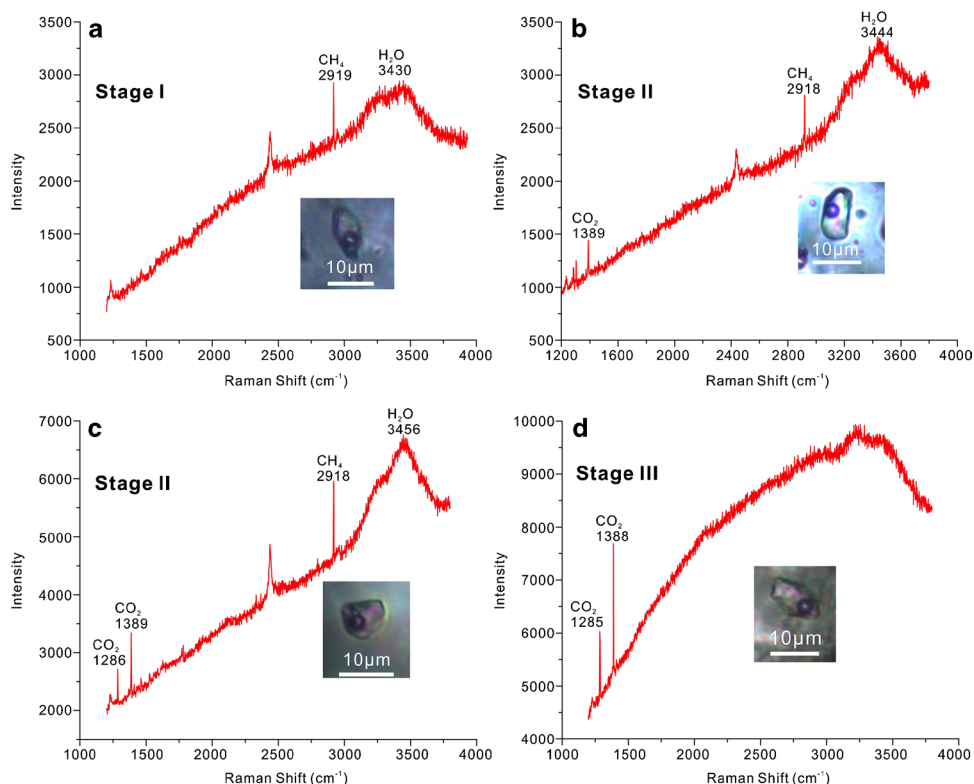


Fig. 8 (a) Plot of $\delta^{18}\text{O}$ versus δD showing the calculated fluid composition of quartz veins. The primary magmatic water field, metamorphic water field, and meteoric water line are from Taylor (1974). SMOW = Standard Mean Ocean Water. (b) Calculated oxygen isotope compositions of waters in equilibrium with different stages of quartz, wolframite, and cassiterite from the Hermyingyi W–Sn deposit

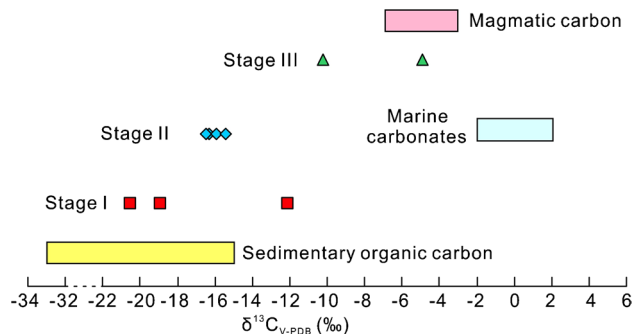


Fig. 9 Carbon isotopic compositions of fluid inclusions in quartz from different mineralization stages in the Hermyingyi W–Sn deposit. Carbon isotopic compositions of igneous rocks, marine carbonates and sedimentary organic matter are cited from Ohmoto (1972) and Hoefs (2009)

average = 2.0‰), chalcopyrite (3.0–3.5‰; $n = 4$, average = 3.2‰), pyrite (2.4–4.5‰; $n = 5$, average = 3.7‰), and sphalerite (2.5–4.3‰; $n = 5$, average = 3.3‰) (ESM Table 3; Fig. 10).

Sulfide minerals have a narrow range of $^{206}\text{Pb}/^{204}\text{Pb}$ (18.655–18.749), $^{207}\text{Pb}/^{204}\text{Pb}$ (15.737–15.768) and $^{208}\text{Pb}/^{204}\text{Pb}$ (39.258–39.368) (ESM Table 4; Fig. 11). Their lead isotope ratios are similar to those of the Hermyingyi monzogranite, with calculated $(^{206}\text{Pb}/^{204}\text{Pb})_t$, $(^{207}\text{Pb}/^{204}\text{Pb})_t$, and $(^{208}\text{Pb}/^{204}\text{Pb})_t$ ratios of 18.572–18.784, 15.749–15.760, and 39.265–39.333, respectively (ESM Table 4; Fig. 11).

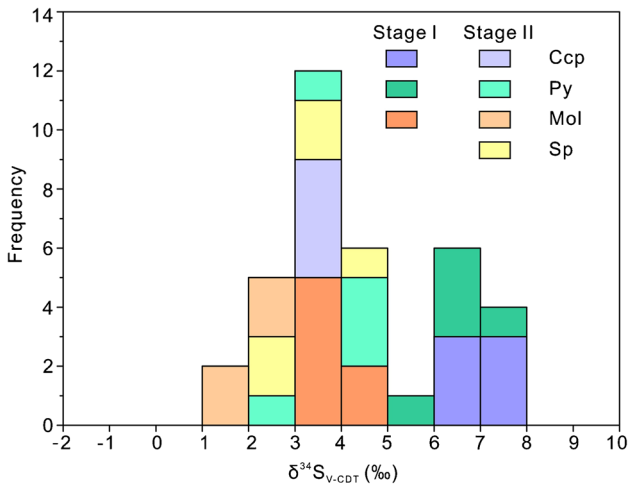


Fig. 10 Histogram of sulfur isotope compositions of sulfides from the Hermyingyi W–Sn deposit. *Ccp* chalcopyrite, *Mol* molybdenite, *Py* pyrite, *Sp* sphalerite

Discussion

Pressure estimation

The microthermometric data of FIs have been widely used in the estimation of fluid trapping pressure and emplacement depth of hydrothermal ore deposits (e.g., Roedder and Bodnar 1980; Rusk et al. 2008). An accurate pressure estimation can be made provided a cluster of FIs are trapped during phase separation (Roedder and Bodnar 1980). At Hermyingyi, no different types of FIs with contrasting salinities but similar homogenization temperatures occur within individual FIA, integrated with the lack of high-salinity FIs (> ~20 wt% NaCl equiv.), arguing against fluid immiscibility or boiling. Under this circumstance, according to Rusk et al. (2008), only the minimum trapping pressure can be determined for the Hermyingyi deposit. Given that the mineralizing fluid at Hermyingyi

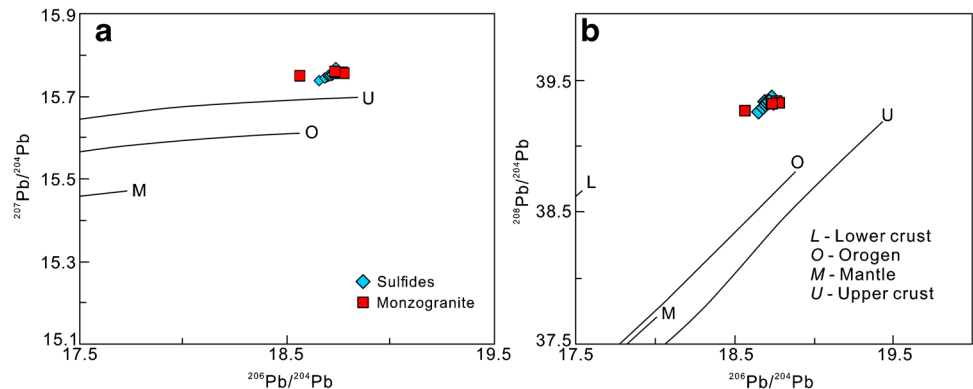
is a simple NaCl–H₂O solution, we calculate the trapping pressure based on the formulae given by Driesner and Heinrich (2007). As shown in Fig. 12 a, the estimated trapping pressures of stage I are 50–200 bars, corresponding to depths of 0.5–2 km, assuming hydrostatic conditions; the trapping pressures of stage II and III are less than 50 bars, corresponding to a depth of < 0.5 km, assuming hydrostatic conditions. Overall, the actual trapping pressures at Hermyingyi would be somewhat higher than these estimated values.

Sources of the mineralizing fluids and metals

Quartz of stage I has δ¹⁸O_{fluid} values of 3.3 to 5.2‰ and δD values of –76 to –61‰, plotting close to the magmatic water field (Fig. 8(a)). In comparison, the δ¹⁸O_{fluid} values for wolframite (4.6 to 5.5‰) and cassiterite (6.0 to 7.0‰) of stage I are slightly higher (ESM Table 2). All these data suggest that the fluid of stage I was dominantly magmatic in origin (Fig. 8). Quartz of stage II has lower δ¹⁸O_{fluid} (1.3–1.8‰) and δD values (–81 to –71‰), lending support to a mixture of magmatic and meteoric water (Fig. 8(a)). Quartz of stage III has the lowest δ¹⁸O_{fluid} (–3.1 to –1.6‰) and δD values (–89 to –73‰), located closer to the meteoric water line (Fig. 8(a)). The general trend to lower δ¹⁸O_{fluid} and δD values with time (Fig. 8) suggests that more meteoric water was involved from stage I to III, and meteoric water has become dominant in stage III.

CO₂ extracted from FIs hosted in quartz has a wide range of carbon isotope values (–20.5 to –4.9‰), exhibiting an increasing trend through time (ESM Table 2; Fig. 9). Previous studies have suggested that the δ¹³C values of CO₂ from quartz-hosted FIs may approximately represent the carbon isotope composition (δ¹³C_{fluid} values) of total carbon in hydrothermal fluids and that variations in δ¹³C_{fluid} values may suggest different carbon sources (Kelly and Rye 1979; Ohmoto 1986). Quartz of stage I has δ¹³C_{CO2} values of –20.5 to –12.1‰, which are intermediate between the characteristic ranges of the organic carbon source

Fig. 11 a, b Lead isotopic compositions of sulfides and granites in the Hermyingyi W–Sn deposit. The Pb isotope curves for the mantle, orogen, and crust are from Zartman and Doe (1981)



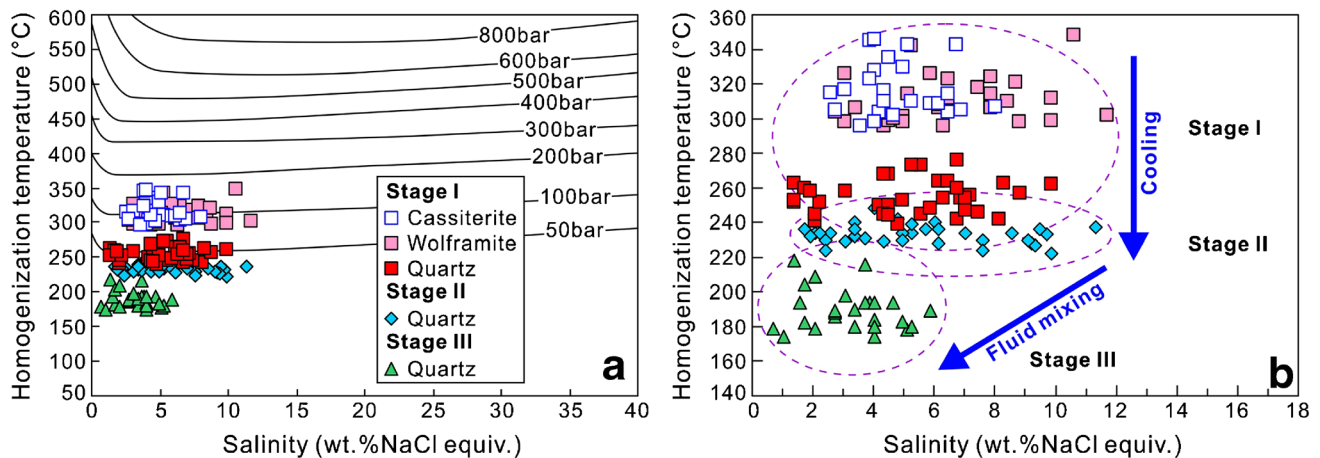


Fig. 12 **a** Pressure estimation for fluid inclusions from different stages. Isobars were calculated from the equations of Driesner and Heinrich (2007). **b** Plot of homogenization temperature versus salin-

ity for fluid inclusions from different mineralization stages in the Hermyingyi W–Sn deposit

in sediments and the magmatic carbon source (Fig. 11), implying a contribution of ^{13}C -depleted organic matter to the hydrothermal system during stage I. By combining the inference of a dominantly magmatic fluid in stage I (Fig. 10), we favor an interpretation that the magmatic fluid of stage I had its carbon isotope signatures modified by the addition of organic carbon, which presumably resulted from the interaction of the magmatic fluid with the surrounding metasedimentary rocks. Greisenization along the ore-bearing veins (Fig. 4b–d), involving the reaction of the fluid with feldspar, provides direct evidence of fluid–rock interaction. This interpretation also corresponds to trace amounts of CH_4 detected in stage I (Fig. 7a–c). According to Dewaele et al. (2016), organic volatiles such as CH_4 , which may have formed through the decomposition of organic matter in sediments, can be released into the hydrothermal system during fluid–rock interaction. As the $\delta^{13}\text{C}_{\text{CO}_2}$ values increase gradually from stage I to III, and quartz of stage III has $\delta^{13}\text{C}_{\text{CO}_2}$ values (-10.2 to -4.9‰) close to the magmatic carbon source (Fig. 9), we suspect that isotopically light organic carbon was consumed with time and almost exhausted in stage III. The consumption of organic matter seems consistent with the observation of the disappearance of CH_4 and the occurrence of CO_2 from stage I to III (Fig. 7), which, as previously documented in the Pedra Preta wolframite deposit (Brazil), has been interpreted as the oxidation of CH_4 to CO_2 under more oxidizing conditions (Rios et al. 2003). The increasing $\delta^{13}\text{C}_{\text{CO}_2}$ values with time (Fig. 9), coupled with oxygen and hydrogen isotope evidence (Fig. 8), indicate that the influx of meteoric water may have contributed to increasing oxygen fugacity ($f\text{O}_2$).

The lack of sulfate minerals combined with the detection of CH_4 in some FIs (Fig. 7a–c) suggests a relatively reduced condition in which H_2S was the dominant sulfur

species (Ohmoto 1972). The bulk sulfur isotope composition of the hydrothermal system can thus be well approximated by $\delta^{34}\text{S}$ values of sulfides (Ohmoto 1972). Sulfides from stage I and II have $\delta^{34}\text{S}$ values ranging from 3.2 to 7.9‰ and from 1.6 to 4.5‰, respectively, implying a relatively homogeneous sulfur source (ESM Table 3; Fig. 10). There is a decreasing trend in $\delta^{34}\text{S}$ values from stage I to II, which may be attributed to increasing pH and/or $f\text{O}_2$ (Ohmoto 1972). An increase in pH is likely since the accompanied greisenization is a reaction involving the consumption of H^+ ions (Heinrich 1990; Pirajno 2009), which would provoke an increase in pH. Increasing $f\text{O}_2$ is also the cause, which agrees well with the oxidation of CH_4 to CO_2 as shown by laser Raman analyses (Fig. 7a–c), abundant sulfide deposition, and the input of oxidized meteoric water in stage II. Of course, a modest increase in $f\text{O}_2$ is suggested, given that a significant change in $f\text{O}_2$ would result in sulfate deposition (Ohmoto 1972), contrary to the observation at Hermyingyi. The relatively limited range of $\delta^{34}\text{S}$ values (1.6–7.9‰) at Hermyingyi, similar to those reported for granite-related W–Sn deposits worldwide, such as the Mawchi deposit in Myanmar ($\delta^{34}\text{S} = -3.6$ to 5.0‰; Myint et al. 2018), the Panasqueira deposit in Portugal ($\delta^{34}\text{S} = -4.0$ to 3.0‰; Kelly and Rye 1979), and the Shirenzhang ($\delta^{34}\text{S} = -5.7$ to -2.9‰), Meiziwo ($\delta^{34}\text{S} = -7.0$ to -3.3‰), and Yaoling ($\delta^{34}\text{S} = -4.1$ to 0.3‰) deposits in China (Jiang et al. 2019b), indicates a magmatic origin for sulfur, e.g., the local Hermyingyi granitic magma.

At Hermyingyi, the limited range of Pb isotopic compositions of sulfides indicates an isotopically homogeneous source (ESM Table 4; Fig. 11). The Hermyingyi monzogranite has age-corrected Pb isotope ratios comparable to the sulfides, with all data plotting above the upper continental crust curve on the Pb–Pb diagram (Fig. 11). Together with

the spatial and temporal proximity between the ore-bearing veins and the monzogranite (Jiang et al. 2017, 2019a), it is reasonable to consider the Hermyingyi monzogranite as the likely source of ore lead.

Fluid evolution

It has been suggested that quartz vein-type W–Sn deposits are genetically associated with highly evolved granites, from which aqueous fluids would have exsolved during the magmatic-hydrothermal transition, which are the possible source of metals (Heinrich 1990; Wood and Samson 2000; Pirajno 2009; Hulsbosch et al. 2016; Jiang et al. 2017, 2018, 2019a, 2019b, 2020; Lehmann 2021; Ni et al. 2020). At Hermyingyi, the close spatial and temporal association of W–Sn mineralization with granitic magmatism has been well documented (Jiang et al. 2017, 2019a). The Hermyingyi monzogranite has high F contents (0.02–0.65 wt%) and extremely low Nb/Ta ratios (1.98–4.04) (Jiang et al. 2017), most likely resulting from a combination of fractional crystallization and the exsolution of volatile-rich fluids (Jahn et al. 2001; Ballouard et al. 2016).

At Hermyingyi, the hydrothermal system has gone through a three-stage process comprising the wolframite-cassiterite stage (stage I), the sulfide stage (stage II), and the barren quartz vein stage (stage III) (Fig. 3). The H₂O–NaCl system is indicated by laser Raman analysis, in which trace amounts of volatiles (e.g., CH₄ and CO₂) were dissolved (Fig. 7). Overall, the mineralizing fluids were of low salinity (0.7–11.7 wt% NaCl equiv.) and medium–low temperature (174–348 °C). In stage I, FIs in quartz have T_h of 241–276 °C and salinities of 1.4–9.9 wt% NaCl equiv.; FIs in wolframite and cassiterite have similar salinities, but their temperatures are ~60 °C higher than those in the coexisting quartz (ESM Table 1; Figs. 6(a–d) and 12b). Such a large temperature gap between coexisting wolframite, cassiterite, and quartz has been previously reported from many W–Sn deposits worldwide, especially those in China (Wei et al. 2012; Ni et al. 2015; Chen et al. 2018; Myint et al. 2018). The temperature gap, previously ascribed to the reversible post-trapping effect which may result in only a small temperature error for FIs trapped in quartz (Roedder 1984), is reinterpreted by some researchers to represent the true temperature difference, indicating the earlier deposition of wolframite than the coexisting quartz (Lüders 1996; Ni et al. 2015). The interpretation of Lüders (1996) and Ni et al. (2015) is plausible for the microthermometric data obtained herein as well, especially considering the field evidence that both wolframite and cassiterite occur mainly along the vein walls (Fig. 4b, c). Based on hydrogen, oxygen, and carbon isotope data, it is inferred that the fluid of stage I was dominantly of magmatic origin, and its carbon isotope values

were modified by addition of organic carbon through fluid–rock interaction (Figs. 8 and 9).

In stage II, FIs in quartz have T_h of 222–248 °C and salinities of 1.7–11.3 wt% NaCl equiv. (ESM Table 1; Fig. 6(e, f)). From stages I to II, a visible decrease in temperatures is observed accompanied by nearly constant salinities (Fig. 12b). We argue that this trend may only record the cooling process of the mineralizing fluid from stages I to II, and may imply that the influence of fluid mixing was minor, despite decreasing $\delta^{18}\text{O}_{\text{fluid}}$ and δD values indicating the influx of small amounts of meteoric water (Fig. 8(a)). Slightly higher $\delta^{13}\text{C}_{\text{CO}_2}$ values of quartz in stage II as compared to quartz in stage I (Fig. 9) are ascribed to the consumption of ¹³C-depleted organic matter.

FIs in quartz of stage III have lowest T_h (174–218 °C) and salinities (0.7–5.9 wt% NaCl equiv.) (ESM Table 1; Fig. 6(g, h)). From stages II to III, there is a drop in both temperatures and salinities (Fig. 12b), which can be readily explained by progressive cooling and dilution by increasing amounts of meteoric water, as shown by hydrogen and oxygen isotope evidence (Fig. 8(a)). The $\delta^{13}\text{C}_{\text{CO}_2}$ values close to the magmatic carbon source (Fig. 9) possibly indicate the almost exhaustion of organic matter in stage III.

Ore deposition mechanism

At Hermyingyi, fluid cooling may have facilitated wolframite deposition. Our microthermometric results obtained from stage I reveal that the fluid experienced a decrease in temperature accompanied by nearly constant salinity (Fig. 12b). This trend contrasts with cooling and dilution by mixing with meteoric water (Wilkinson 2001; Wei et al. 2012; Jiang et al. 2019b) but may be explained by a simple cooling process, which could significantly reduce the temperature but is unable to change the salinity (Wilkinson 2001; Ni et al. 2015; Chen et al. 2018). Hydrogen and oxygen isotope data of quartz combined with oxygen isotope data of wolframite and cassiterite (Fig. 8) also argue against the involvement of meteoric water in stage I. Three reasons render it unlikely that fluid boiling, if any, was a dominant wolframite deposition at Hermyingyi. Firstly, boiling assemblages consisting of coexisting brine and vapor phases, which serve as the direct and solid evidence for fluid boiling, are lacking in stage I (ESM Fig. 2). Secondly, the salinities of the mineralizing fluid of stage I are low and range from 1.4 to 11.7 wt% NaCl equiv., similar to those (0–15 wt% NaCl equiv.) reported for W(–Sn) deposits worldwide which are not produced by the fluid boiling process (e.g., Wood and Samson 2000), such as Panasquiera in Portugal (4.5–11.2 wt% NaCl equiv.; Kelly and Rye 1979), Dae Hwa in Korea (2.6–14.4 wt% NaCl equiv.; So et al. 1983), Xihuashan (0.9–13.7 wt% NaCl equiv.; Wei et al. 2012), and Dajishan in China (0.2–8.8 wt% NaCl equiv.; Ni et al. 2015), and Mawchi in

Myanmar (4.5–15.7 wt% NaCl equiv.; Myint et al. 2018). Of note, according to Korges et al. (2018), such a salinity variation (1–10 wt% NaCl equiv.) may reflect gentle boiling. Thirdly, unlike the Hermyingyi deposit, the W–Sn deposits produced by the fluid boiling process contain high-salinity FIs (> ~20 wt% NaCl equiv.), which mostly homogenize through halite dissolution (Wood and Samson 2000). For example, the Sn–W Zinnwald deposit contains brine inclusions with salinities up to 40 wt% NaCl equiv. (Korges et al. 2018). The highly depleted $\delta^{13}\text{C}_{\text{CO}_2}$ values indicate fluid–rock interaction in stage I (Fig. 9), as revealed by the accompanied greisenization along the ore-bearing quartz veins (Fig. 4b–d; Jiang et al. 2019a). Fluid–rock interaction seems a viable mechanism for wolframite deposition because (1) external Fe and Mn are required to precipitate wolframite from fluids with tungstate species such as H_2WO_4^0 , HWO_4^- , WO_4^{2-} , NaHWO_4^0 , and NaWO_4^- which are dominantly responsible for tungsten transport (Wood and Samson 2000; Wang et al. 2019); (2) the thermodynamic simulation study of Wang et al. (2020) revealed that aqueous tungsten could maintain its mobility only insofar as the hydrothermal fluid contains extremely low contents of Fe, Mn, and Ca; and (3) Lecumberri-Sanchez et al. (2017) argued that as a result of fluid–rock interaction, significant amounts of Fe and Mn (especially Fe) are extracted from the surrounding rocks which provide sufficient Fe and Mn for wolframite deposition. Moreover, the accompanied greisenization, direct evidence for fluid–rock interaction, is an acid-consuming reaction (Heinrich 1990; Pirajno 2009) that may trigger wolframite precipitation by increasing the pH value (Wood and Samson 2000). Considering that the ore-bearing veins are associated with intense greisenization, we speculate that a temperature decrease in stage I may be dominantly caused by heat transfer due to fluid–rock interaction. Of course, the contribution of fluid–rock interaction to wolframite deposition is an issue that deserves further examination, given the proposal of Pan et al. (2019) that the Fe content of the hydrothermal fluid may have been underestimated due to the relatively high detection limit for Fe in LA-ICP-MS.

FIs in cassiterite have similar temperatures but a smaller range of salinities compared to FIs in wolframite (Figs. 6(a, b) and 12). These data, combined with the observations that wolframite crosscuts cassiterite (Fig. 5d) and that cassiterite has higher $\delta^{18}\text{O}_{\text{fluid}}$ values than wolframite (Fig. 8(b)), indicate that cassiterite was probably deposited slightly earlier than wolframite in the Hermyingyi deposit. Fluid–rock interaction is an intriguing mechanism because (1) greisenization is an acid-consuming process that could balance the acidity released during cassiterite deposition; and (2) greisenization would result in preferential oxidation of Sn(II) to Sn(IV) (Heinrich 1990; Pirajno 2009; Hulsbosch et al. 2016; Lehmann 2021). The larger range of salinities of FIs in wolframite may be due to an increase of Na^+

and Cl^- caused by feldspar destruction during continued fluid–rock interaction (e.g., greisenization): $3\text{NaAlSi}_3\text{O}_8$ (feldspar) + 2HCl^0 + $\text{KCl}^0 = \text{KAl}_3\text{Si}_3\text{O}_{10}(\text{OH})_2$ (muscovite) + 6SiO_2 + 3Na^+ + 3Cl^- (Heinrich 1990). Moreover, a temperature decrease due to fluid cooling (Fig. 12b) may promote cassiterite deposition by lowering the solubility of Sn(II)–Cl complexes at Hermyingyi, as previously suggested by Eugster (1986). In summary, it is concluded that both fluid–rock interaction and fluid cooling are efficient mechanisms for wolframite and cassiterite deposition at Hermyingyi.

Conclusions

A study of fluid inclusions in wolframite, cassiterite, and quartz, and C–H–O–S–Pb isotope analysis, is conducted to trace the source of metals and mineralizing fluids and to decipher the ore deposition mechanism in the Hermyingyi quartz vein-type W–Sn deposit. Overall, the mineralizing fluids were of low salinity and medium–low temperature, with trace amounts of dissolved CH_4 and CO_2 . Conventional and infrared microthermometric results suggest that homogenization temperatures of fluid inclusions decrease gradually from stage I to III, whereas their salinities vary in a similar for stages I and II and fall in stage III; fluid inclusions in wolframite and cassiterite from stage I have similar salinities but distinctly higher temperatures compared to those in coexisting quartz. Oxygen and hydrogen isotope values indicate a dominantly magmatic fluid in stage I, which was cooled and diluted by influx of meteoric water in stages II and III. The negative and increasing carbon isotope values imply that organic carbon was added to the magmatic fluid through fluid–rock interaction in stage I, consumed with time, and almost exhausted in stage III. Sulfur and lead isotope values indicate a magmatic origin for sulfur and lead. These new results collectively suggest that fluid–rock interaction and fluid cooling were the driving mechanisms for wolframite and cassiterite deposition in the Hermyingyi W–Sn deposit.

Supplementary Information The online version contains supplementary material available at <https://doi.org/10.1007/s00126-022-01099-y>.

Acknowledgements We are very grateful to Tenwin-Pacific Brothers Mining Services Company Limited for the field assistance. The authors are very grateful to Editor-in-Chief Bernd Lehmann and Associate Editor De-Gao Zhai for the editorial handling and constructive comments of this paper. Lin Hou, Marta Codeço, and an anonymous reviewer are thanked for their constructive reviews, which improved this paper significantly.

Authors contribution Hai Jiang: investigation, writing—original draft; Shao-Yong Jiang: resources, supervision, funding acquisition, writing—review and editing; Wen-Qian Li: investigation; Kui-Dong Zhao:

investigation, methodology; Wei Zhang: investigation, methodology; Qiang Zhang: investigation, methodology.

Funding This study is supported by the National Natural Science Foundation of China (No. 91755208, 41503043, 92162323) and the MOST Special Fund from the State Key Laboratory of Geological Processes and Mineral Resources, China University of Geosciences (No. MSFGPMR03-2).

Availability of data and material All the data are available in the ESM Tables 1–4.

Declarations

Ethics approval and consent to participate Not applicable.

Consent for publication Not applicable.

Competing interests The authors no competing interests.

References

- Balouard C, Poujo M, Boulvais P, Branquet Y, Tartèse R, Vigneresse JL (2016) Nb-Ta fractionation in peraluminous granites: a marker of the magmatic-hydrothermal transition. *Geology* 44:231–234
- Barber AJ, Crow MJ (2009) Structure of Sumatra and its implications for the tectonic assembly of Southeast Asia and the destruction of Paleotethys. *Isl Arc* 18:3–20
- Chen LL, Ni P, Li WS, Ding JY, Pan JY, Wang GG, Yang YL (2018) The link between fluid evolution and vertical zonation at the Maoping tungsten deposit, Southern Jiangxi, China: fluid inclusion and stable isotope evidence. *J Geochem Exploration* 192:18–32
- Cobbing EJ, Mallick DIJ, Pitfield PEJ, Teoh LH (1986) The granites of the southeast Asian tin belt. *J Geol Soc London* 143:537–550
- Cong F, Wu FY, Li WC, Sein K (2021) Petrogenesis of the Main Range and Eastern Province granites in eastern Myanmar: new insights from zircon U-Pb ages and Sr-Nd isotopes. *Lithos* 382–383:105895
- Dewaele S, De Clercq F, Hulsbosch N, Piessens K, Boyce A, Burgess R, Muchez P (2016) Genesis of the vein-type tungsten mineralization at Nyakabingo (Rwanda) in the Karagwe-Ankole belt, Central Africa. *Miner Deposita* 51:283–307
- Driesner T, Heinrich CA (2007) The system H₂O-NaCl. Part I: correlation formulae for phase relations in temperature-pressure-composition space from 0 to 1000 °C, 0 to 5000 bar, and 0 to 1 X_{NaCl}. *Geochim Cosmochim Acta* 71:4880–4901
- Eugster HP (1986) Minerals in Hot Water Am Mineral 71:655–673
- Gardiner NJ, Robb LJ, Searle MP (2014) The metallogenic provinces of Myanmar. *Appl Earth Sci* 123:25–38
- Gardiner NJ, Searle MP, Morley CK, Whitehouse MP, Spencer CJ, Robb LJ (2016) The closure of Palaeo-Tethys in Eastern Myanmar and Northern Thailand: new insights from zircon U-Pb and Hf isotope data. *Gondwana Res* 39:401–422
- Gardiner NJ, Hawkesworth CJ, Robb LJ, Whitehouse MJ, Roberts NMW, Kirkland CL, Evans NJ (2017) Contrasting granite metallogeny through the zircon record: a case study from Myanmar. *Sci Rep* 7:748
- Goldstein RH, Reynolds TJ (1994) Systematics of fluid inclusions in diagenetic minerals. Society of Sedimentary Geology, SEPM Short Course 31:1–199
- Heinrich CA (1990) The chemistry of hydrothermal tin (-tungsten) ore deposition. *Econ Geol* 85:457–481
- Hoefs J (2009) Stable isotope geochemistry, 6th edn. Springer, Berlin
- Hulsbosch N, Boiron MC, Dewaele S, Muchez P (2016) Fluid fractionation of tungsten during granite-pegmatite differentiation and the metal source of peribatholithic W quartz veins: evidence from the Karagwe-Ankole Belt (Rwanda). *Geochim Cosmochim Acta* 175:299–318
- Jahn BM, Wu FY, Capdevila R, Martineau F, Zhao ZH, Wang YX (2001) Highly evolved juvenile granites with tetrad REE patterns: the Woduhe and Baerzhe granites from the Great Xing'an Mountain in NE China. *Lithos* 59:171–198
- Jiang H, Li WQ, Jiang SY, Wang H, Wei XP (2017) Geochronological, geochemical and Sr-Nd-Hf isotopic constraints on the petrogenesis of Late Cretaceous A-type granites from the Sibumasu Block, Southern Myanmar, SE Asia. *Lithos* 268–271:32–47
- Jiang H, Jiang SY, Li WQ, Zhao KD, Peng NJ (2018) Highly fractionated Jurassic I-type granites and related tungsten mineralization in the Shirenzhang deposit, northern Guangdong, South China: evidence from cassiterite and zircon U-Pb ages, geochemistry and Sr-Nd-Pb-Hf isotopes. *Lithos* 312–313:186–203
- Jiang H, Jiang SY, Li WQ, Zhao KD (2019a) Timing and source of the Hermyingyi W-Sn deposit in southern Myanmar, SE Asia: evidence from molybdenite Re-Os age and sulfur isotopic composition. *J Earth Sci* 30:70–79
- Jiang H, Jiang SY, Li WQ, Peng NJ, Zhao KD (2019b) Fluid inclusion and isotopic (C, H, O, S and Pb) constraints on the origin of late Mesozoic vein-type W mineralization in northern Guangdong, South China. *Ore Geol Rev* 112:103007
- Jiang H, Zhao KD, Jiang SY, Li WQ, Zaw K, Zhang D (2021) Late Triassic post-collisional high-K two-mica granites in Peninsular Thailand, SE Asia: petrogenesis and Sn mineralization potential. *Lithos* 398–300:106290
- Jiang SY, Zhao KD, Jiang H, Su HM, Xiong SF, Xiong YQ, Xu YM, Zhang W, Zhu LY (2020) Spatiotemporal distribution, geological characteristics and metallogenic mechanism for tungsten and tin deposits in China: an overview. *Chin Sci Bull* 65:1–16 ((in Chinese with English abstract))
- Kelly WC, Rye RO (1979) Geologic, fluid inclusion, and stable isotope studies on the tin-tungsten deposits of Panasqueira, Portugal. *Econ Geol* 74:1721–1822
- Korges M, Weis P, Lüders V, Laurent O (2018) Depressurization and boiling of a single magmatic fluid as a mechanism for tin-tungsten deposit formation. *Geology* 46:75–78
- Lecumberri-Sanchez P, Vieira R, Heinrich CA, Pinto F, Wälle M (2017) Fluid-rock interaction is decisive for the formation of tungsten deposits. *Geology* 45:579–582
- Lehmann B (2021) Formation of tin ore deposits: a reassessment. *Lithos* 402–403:105756
- Li JX, Zhang LY, Fan WM, Ding L, Sun YL, Peng TP, Li GM, Sein K (2018) Mesozoic-Cenozoic tectonic evolution and metallogeny in Myanmar: evidence from zircon/cassiterite U-Pb and molybdenite Re-Os geochronology. *Ore Geol Rev* 102:829–845
- Li JX, Fan WM, Zhang LY, Evans NJ, Sun YL, Ding L, Guan QY, Peng TP, Cai FL, Sein K (2019) Geochronology, geochemistry and Sr-Nd-Hf isotopic compositions of Late Cretaceous-Eocene granites in southern Myanmar: petrogenetic, tectonic and metallogenic implications. *Ore Geol Rev* 112:103031
- Lin TH, Mitchell AHG, Chung SL, Tan XB, Tang JT, Oo T, Wu FY (2019) Two parallel magmatic belts with contrasting isotopic characteristics from southern Tibet to Myanmar: zircon U-Pb and Hf isotopic constraints. *J Geol Soc London* 176:574–587
- Linnen RL (1998) Depth of emplacement, fluid provenance and metallogeny in granitic terranes: a comparison of western Thailand with other tin belts. *Miner Deposita* 33:461–476

- Liu CZ, Chung SL, Wu FY, Zhang C, Xu Y, Wang JG, Chen Y, Guo S (2016) Tethyan suturing in Southeast Asia: zircon U-Pb and Hf-O isotopic constraints from Myanmar ophiolites. *Geology* 44:1–4
- Lüders V (1996) Contribution of infrared microscopy to fluid inclusion studies in some opaque minerals (wolframite, stibnite, bournonite): metallogenic implications. *Econ Geol* 91:1462–1468
- Mao W, Zhong H, Yang JH, Tang YW, Liu L, Fu YZ, Zhang XC, Sein K, Aung SM, Li J, Zhang L (2020) Combined zircon, molybdenite, and cassiterite geochronology and cassiterite geochemistry of the Kuntabin tin-tungsten deposit in Myanmar. *Econ Geol* 115:603–625
- Metcalf I (2013) Gondwana dispersion and Asian accretion: tectonic and palaeogeographic evolution of eastern Tethys. *J Asian Earth Sci* 66:1–33
- Mitchell A, Chung SL, Oo T, Lin TH, Hung CH (2012) Zircon U-Pb ages in Myanmar: magmatic-metamorphic events and the closure of a neo-Tethys ocean? *J Asian Earth Sci* 56:1–23
- Myint AZ, Yonezu K, Boyce AJ, Selby D, Scherstén A, Tindell T, Watanabe K, Swe YM (2018) Stable isotope and geochronological study of the Mawchi Sn-W deposit, Myanmar: implications for timing of mineralization and ore genesis. *Ore Geol Rev* 95:663–679
- Ng SWP, Chung SL, Robb LJ, Ghani AA, Chung SL, Oliver GJH, Sone M, Gardiner NJ, Roselee MH (2015) Petrogenesis of Malaysian granitoids in the Southeast Asian tin belt: part 2. U-Pb zircon geochronology and tectonic model. *Geol Soc Am Bull* 127:1238–1258
- Ni P, Wang XD, Wang GG, Huang JB, Pan JY, Wang TG (2015) An infrared microthermometric study of fluid inclusions in coexisting quartz and wolframite from Late Mesozoic tungsten deposits in the Gannan metallogenic belt, South China. *Ore Geol Rev* 65:1062–1077
- Ni P, Li WS, Pan JY (2020) Ore-forming fluid and metallogenic mechanism of wolframite-quartz vein-type tungsten deposits in South China. *Acta Geol Sin-Engl* 94:1774–1796
- Ohmoto H (1972) Systematics of sulfur and carbon isotopes in hydrothermal ore deposits. *Econ Geol* 67:551–579
- Ohmoto H (1986) Stable isotope geochemistry of ore deposits. In: Valley JH, Taylor HP Jr, O'Neil JR (eds) Stable isotopes in high temperature geological processes. *Rev Mineral* 16:491–559
- Pan JY, Ni P, Wang RC (2019) Comparison of fluid processes in coexisting wolframite and quartz from a giant vein-type tungsten deposit, South China: insights from detailed petrography and LA-ICP-MS analysis of fluid inclusions. *Am Mineral* 104:1092–1116
- Peng NJ, Jiang SY, Xiong SF, Pi DH (2018) Fluid evolution and ore genesis of the Dalingshang deposit, Dahutang W-Cu ore field, northern Jiangxi Province, South China. *Miner Deposita* 51:1–16
- Pirajno F (2009) *Hydrothermal processes and mineral systems*. Springer, Berlin
- Ridd MF (2009) The Phuket Terrane: a Late Palaeozoic rift at the margin of Sibumasu. *J Asian Earth Sci* 36:238–251
- Rios FJ, Villas RN, Fuzikawa K (2003) Fluid evolution in the Pedra Preta wolframite ore deposit, Paleoproterozoic Musa granite, eastern Amazon craton, Brazil. *J South Am Earth Sci* 15:787–802
- Roedder E (1984) Fluid Inclusions *Rev Mineral* 12:1–644
- Roedder E, Bodnar R (1980) Geologic pressure determinations from fluid inclusion studies. *Annu Rev Earth Planet Sci* 8:263–301
- Romer RL, Kroner U (2016) Phanerozoic tin and tungsten mineralization-tectonic controls on the distribution of enriched protoliths and heat sources for crustal melting. *Gondwana Res* 31:60–95
- Rusk BG, Reed MH, Dilles JH (2008) Fluid inclusion evidence for magmatic-hydrothermal fluid evolution in the porphyry copper-molybdenum deposits at Butte, Montana. *Econ Geol* 103:307–334
- Schwartz MO, Rajah SS, Askury AK, Putthapiban P, Djaswadi S (1995) The southeast Asian tin belt. *Earth-Sci Rev* 38:95–293
- Searle MP, Noble SR, Cottle JM, Waters DJ, Mitchell AHG, Hlaing T, Horstwood MSA (2007) Tectonic evolution of the Mogok metamorphic belt, Burma (Myanmar) constrained by U-Th-Pb dating of metamorphic and magmatic rocks. *Tectonics* 26:TC3014
- So CS, Shelton KL, Seidemann DE, Skinner BJ (1983) The Dae Hwa tungsten-molybdenum mine, Republic of Korea: a geochemical study. *Econ Geol* 78:920–930
- Taylor HP Jr (1974) The application of oxygen and hydrogen isotope studies to problems of hydrothermal alteration and ore deposition. *Econ Geol* 69:843–883
- Than Htun, Than Htay, Khin Zaw (2017) Tin-tungsten deposits of Myanmar. In: Barber AJ, Khin Zaw, Crow MJ (eds) Myanmar: geology, resources and tectonics. Geological Society, London, *Memoirs* 48:625–647
- Wang JG, Wu FY, Tan XC, Liu CZ (2014) Magmatic evolution of the Western Myanmar Arc documented by U-Pb and Hf isotopes in detrital zircon. *Tectonophysics* 612–613:97–105
- Wang XL, Qiu Y, Lu JJ, Chou IM, Zhang WL, Li GL, Hu WX, Li Z, Zhong RC (2020) In situ Raman spectroscopic investigation of the hydrothermal speciation of tungsten: implications for the ore-forming process. *Chem Geol* 532:119299
- Wang XS, Timofeev A, Williams-Jones AE, Shang LB, Bi XW (2019) An experimental study of the solubility and speciation of tungsten in NaCl-bearing aqueous solutions at 250, 300, and 350 °C. *Geochim Cosmochim Acta* 265:313–329
- Wei WF, Hu RZ, Bi XW, Peng JT, Su WC, Song SQ, Shi SH (2012) Infrared microthermometric and stable isotopic study of fluid inclusions in wolframite at the Xihuashan tungsten deposit, Jiangxi province, China. *Miner Deposita* 47:589–605
- Wilkinson JJ (2001) Fluid inclusions in hydrothermal ore deposits. *Lithos* 55:229–272
- Wood SA, Samson IM (2000) The hydrothermal geochemistry of tungsten in granitoid environments: I. Relative solubilities of ferberite and scheelite as a function of T, P, pH and m(NaCl). *Econ Geol* 95:143–182
- Yang JH, Zhou MF, Hu RZ, Zhong H, Williams-Jones AE, Liu L, Zhang XC, Fu YZ, Mao W (2020) Granite-related tin metallogenic events and key controlling factors in Peninsular Malaysia, Southeast Asia: new insights from cassiterite U-Pb dating and zircon geochemistry. *Econ Geol* 115:581–601
- Zartman RE, Doe BR (1981) Plumbotectonics—the model. *Tectonophysics* 75:135–162
- Zhang J, Chen YJ, Pirajno F, Deng J, Chen HY, Wang CM (2013) Geology, C-H-O-S-Pb isotope systematics and geochronology of the Yindongpo gold deposit, Tongbai Mountains, central China: implication for ore genesis. *Ore Geol Rev* 53:343–356

Publisher's note Springer Nature remains neutral with regard to jurisdictional claims in published maps and institutional affiliations.